h-AlN-$Mg(OH)_2$ van der Waals bilayer heterostructure: Tuning the excitonic characteristics

C. Bacaksiz,[1] A. Dominguez,[2] A. Rubio,[2,3] R. T. Senger,[1] and H. Sahin[4]
[1]*Department of Physics, Izmir Institute of Technology, 35430 Izmir, Turkey*
[2]*Max Planck Institute for the Structure and Dynamics of Matter, and Center for Free-Electron Laser Science, Luruper Chaussee 149, 22761 Hamburg, Germany*
[3]*Nano-Bio Spectroscopy Group and ETSF, Department Fisica de Materiales, Universidad del Pais Vasco, CFM CSIC-UPV/EHU-MPC and DIPC, 20018 San Sebastian, Spain*
[4]*Department of Photonics, Izmir Institute of Technology, 35430 Izmir, Turkey*
(Received 14 October 2016; revised manuscript received 20 January 2017; published 21 February 2017)

Motivated by recent studies that reported the successful synthesis of monolayer $Mg(OH)_2$ [Suslu *et al.*, Sci. Rep. **6**, 20525 (2016)] and hexagonal (*h*-)AlN [Tsipas *et al.*, Appl. Phys. Lett. **103**, 251605 (2013)], we investigate structural, electronic, and optical properties of vertically stacked *h*-AlN and $Mg(OH)_2$, through *ab initio* density-functional theory (DFT), many-body quasiparticle calculations within the GW approximation and the Bethe-Salpeter equation (BSE). It is obtained that the bilayer heterostructure prefers the AB' stacking having direct band gap at the Γ with Type-II band alignment in which the valance band maximum and conduction band minimum originate from different layer. Regarding the optical properties, the imaginary part of the dielectric function of the individual layers and heterobilayer are investigated. The heterobilayer possesses excitonic peaks, which appear only after the construction of the heterobilayer. The lowest three exciton peaks are analyzed in detail by means of band decomposed charge density and the oscillator strength. Furthermore, the wave function calculation shows that the first peak of the heterobilayer originates from spatially indirect exciton where the electron and hole localized at *h*-AlN and $Mg(OH)_2$, respectively, which is important for the light harvesting applications.

DOI: 10.1103/PhysRevB.95.075423

I. INTRODUCTION

After the discovery of graphene [1], interest in atomically thin materials [2] has grown rapidly due to their extraordinary physical properties [3,4]. In the past decade, several 2D materials have been synthesized and theoretically predicted, such as silicene [5,6], germanene [5], stanene [7,8], transition metal dichalcogenides (TMDs such as MoS_2, WS_2) [9–16], and III-V binary compounds (e.g., *h*-BN, *h*-AlN) [17–21]. Beside the single crystal of 2D materials, recently emerging field is their vertically stacked heterostructures [22]. Because of the van der Waals-type weak interlayer interaction, the synthesis of heterostructures is not restricted with the lattice matching of each layer. This provides a wide variety of combinations of layers, which exhibit different electronic and optical properties [23–29].

Stable hexagonal crystalline structure of AlN was first theoretically predicted by Sahin *et al.* [17] and experimentally synthesized by Tsipas *et al.* [20]. They found that, differing from its bulk structure, which is an insulator, monolayer *h*-AlN is a semiconductor with the indirect band gap where the valance band maximum and conduction band minimum at the K and Γ points, respectively. Almeida *et al.* [30] investigated properties of defects, such as vacancies, antisites, and impurities, in *h*-AlN. It was reported that N vacancies and Si impurities lead to the breaking of the planar symmetry and cause significant changes in the electronic properties. Shi *et al.* [31] calculated the magnetic properties of bare and transition-metal (TM) doped AlN nanosheets by using first-principles calculations. They reported that nonmagnetic *h*-AlN can be magnetized upon a single TM atom. Moreover, the electronic structures of nanoribbon of AlN were investigated by Zheng *et al.* [32] and it is predicted that zig-zag edge nanoribbons have an indirect band gap while armchair edge nanoribbons have a direct band gap, and band gaps of both zig-zag and armchair decrease monotonically with increasing ribbon width. Furthermore, Bacaksiz *et al.* [21] reported that the electronic band structure changes significantly when the number of layers increases and the structure having 10 or more layers exhibits direct bandgap as bulk form. More recently, Kecik *et al.* [33] investigated the optical properties of mono- and few-layer *h*-AlN under strain. They reported that the absorption peaks stand outside the visible-light regime; on the other hand, the applied tensile strain gradually redshifts the optical spectra.

As a constituent of heterobilayer, physical properties of $Mg(OH)_2$ were investigated previously in several studies [34–36]. It is a layered metal hydroxide with a wide band gap [37]. As a member of the alkaline-earth-metal hydroxides (AEMHs) family, $Ca(OH)_2$ was predicted to be stable in the bilayer and monolayer forms by Aierken *et al.* [38]. In addition, Torun *et al.* investigated the optical properties of GaS–$Ca(OH)_2$ bilayer heterostructure by using GW+BSE and reported that in spite of the similarities of electronic structures, the different stacking types have different optical spectra [39]. Recently, Tsukanov *et al.* investigated the interaction of organic anions with layered double hydroxide nanosheets consisting of Mg and Al by using molecular dynamics simulations [40]. In addition, very recently, the monolayer $Mg(OH)_2$ was synthesized and reported that in spite of the optically inactive nature of $Mg(OH)_2$, the photoluminescence intensity of monolayer MoS_2 was assisted by $Mg(OH)_2$ and enhanced [41]. Most recently, Yagmurcukardes *et al.* investigated the heterobilayer of the $Mg(OH)_2$ and WS_2 [42]. They reported that the lower energy optical spectrum of the $Mg(OH)_2$–WS_2 heterobilayer is dominated by the excitons originates WS_2

 ©2017 American Physical Society

layers. These two studies indicate that the $Mg(OH)_2$ is a candidate for tuning the optical property of other monolayer materials.

In the present work, the heterostructure of two perfectly matching monolayers of *h*-AlN, a member of III-V binary compounds, and $Mg(OH)_2$, a member of alkaline-earth-metal hydroxide (AEMH), are considered. The similar lattice constants of the layers allow us to use smaller supercell, which is important especially for calculating the optical properties. We found that the vertically stacked heterostructure possesses excitonic peaks, which appear only after the construction of the heterobilayer. More significantly, the wave function calculation shows that the first peak of the imaginary part of the dielectric function for the heterobilayer originates from spatially indirect exciton where the electron and hole localized at *h*-AlN and $Mg(OH)_2$, respectively.

The paper is organized as follows: In Sec. II we give details of our computational methodology. In Sec. III we present a brief overview of the structural and electronic properties of monolayer *h*-AlN and $Mg(OH)_2$. In Sec. IV different stacking orders of bilayer heterostructure of *h*-AlN and $Mg(OH)_2$ and also optical property of the energetically favorable stacking order are investigated in detail. Finally, we present our conclusion in Sec. V.

II. COMPUTATIONAL METHODOLOGY

Employing (DFT)-based methods, we investigated the structural, electronic, and optical properties of monolayer *h*-AlN and $Mg(OH)_2$ and their heterobilayers. We used the Vienna *ab initio* simulation package VASP [43–45], which solves the Kohn-Sham equations iteratively using a plane-wave basis set. To describe electron exchange and correlation, the Perdew-Burke-Ernzerhof (PBE) form of the generalized gradient approximation (GGA) [46] was adopted. The van der Waals (vdW) forces, which is important for layered materials, was taken into account by using the DFT-D2 method of Grimme [47,48]. To obtain partial charge on the atoms, a Bader charge analysis was used [49].

Structural optimizations were performed with the following parameters. The kinetic energy cutoff of the plane-wave basis set was 500 eV in all calculations. The total energy difference between the sequential steps in the iterations was taken 10^{-5} units as convergence criterion. The convergence for the Hellmann-Feynman forces per unit cell atom was taken to be 10^{-4} eV/Å. Gaussian smearing of 0.05 eV was used and the pressures on the unit cell were decreased to a value less then 1.0 kB in all three directions. For the determination of accurate charge densities, Brillouin zone integration was performed using a $35\times35\times1$ Γ-centered mesh for the primitive unit cell. To avoid interactions between adjacent monolayer and heterobilayers, our calculations were performed with a large unit cell including ~18 Å vacuum space. We also calculated the cohesive energy (E_{coh}), which was formulated as $E_{coh} = [(\sum_i n_i E_i) - E_T]/\sum_i n_i$, where i stands for the atoms which contract the structure; n_i, E_i, and E_T are the number of i atom in the unit cell, the energy of free i atom, and the total energy per unit cell, respectively.

In addition, the quasiparticle (QP) energies were calculated within the GW_0 approximation where the single-particle Green function part (G) was iterated and the screened Coulomb interaction part (W) was fixed. On top of GW_0 approximation, the energies of two-particle system of quasielectron and quasihole (exciton) were calculated by solving BSE [50,51]. To obtain accurate QP states, 320 bands were considered in the GW_0 calculations. Our convergence tests showed that the $12\times12\times1$ k-point sampling and the vacuum spacing of ~28 Å well approximates the excitonic properties of vdw heterobilayer structure (see Appendix). The eight highest valence bands and lowest conduction bands were considered as a basis for the excitonic states.

III. SINGLE LAYER *h*-AlN and $Mg(OH)_2$

Before analysis of bilayer heterostructure of *h*-AlN and $Mg(OH)_2$, the monolayer constituents are discussed. First, the monolayer structure of *h*-AlN [see Fig. 1(a)] belongs to space group $P6_3/mmc$ with the lattice constant 3.13 Å, which is consistent with that of few-layer hexagonal AlN that reported by Tsipas and the coworkers [20]. In Table I, the number of valance electrons of the isolated single atom and of the one in

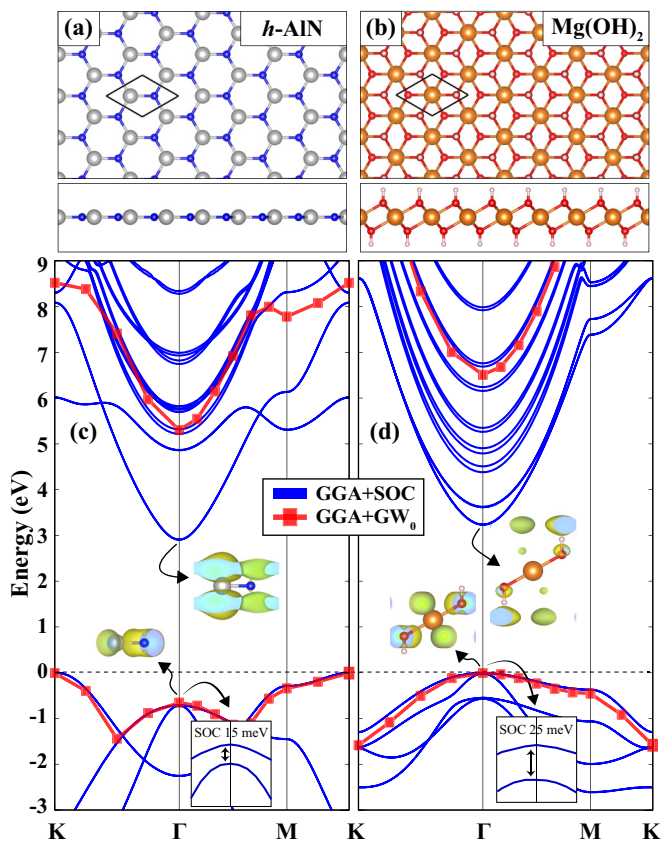

FIG. 1. Upper panel illustrates the structure of monolayer *h*-AlN (left) and $Mg(OH)_2$ (right). (a) and (b) are the structures (top and side view), and the solid black parallelograms show the unit cell of the structure; (c) and (d) are the band structures of *h*-AlN and $Mg(OH)_2$, respectively. The blue and light-red curves with square are for GGA+SOC and GGA+GW_0, respectively. The dashed vertical line is shows the Fermi energy. In the band diagram, the charge densities of the VBM and CBM and the spin-orbit splitting at the Γ point.

TABLE I. Calculated parameters for monolayer h-AlN and Mg(OH)$_2$ are the lattice constant in the lateral direction, a; the final charges of Al, N, Mg, O, and H, ρ_{Al}, ρ_N, ρ_{Mg}, ρ_O, ρ_H, respectively; the work function Φ; the cohesive energy, E_{coh}; and the spin-orbit splitting, Δ_{SO}. E_g^{GGA} and $E_g^{GW_0}$ are the energy band gap values within GGA+SOC and GGA+GW$_0$, respectively.

	a (Å)	ρ_{Al} (e^-)	ρ_N (e^-)	ρ_{Mg} (e^-)	ρ_O (e^-)	ρ_H (e^-)	Φ (eV)	E_{coh} (eV)	E_g^{GGA} (eV)	Δ_{SO} (meV)	$\Gamma \to \Gamma$ (eV)	$K \to K$ (eV)	$E_g^{GW_0}$ (eV)
h-AlN	3.13	0.7	7.3	—	—	—	5.12	5.35	2.90	15	3.62	6.02	5.37 (K-Γ)
Mg(OH)$_2$	3.13	—	—	0.3	7.4	0.4	4.20	4.38	3.23	25	3.23	8.92	6.51 (Γ-Γ)

crystal are given. It is seen that Al donates 2.3 of 3.0 e^- to N, which indicates that the bond between Al and N have strong ionic character. The work function is found to be 5.12 eV. As shown in Fig. 1(c), h-AlN has an indirect band gap of 2.9 eV, where the valance band maximum (VBM) and the conduction band minimum (CBM) are at the Γ and K points, respectively. GW$_0$ band gap is calculated to be 5.30 eV. In addition, differing from similar TMDs, the spin-orbit (SO) splitting at the Γ point is quite small (15 meV) [52].

Structural and electronic properties of monolayer Mg(OH)$_2$, which is another building-block of heterobilayer are also presented in Figs. 1(b) and 1(d). The lattice parameter of Mg(OH), which belongs to $P\bar{3}m1$ space group is found to be 3.13 Å. Therefore, it perfectly matches to h-AlN. Upon the formation of this crystalline structure In this structure: (i) Mg donates almost all valance electrons, 1.8 of 2.0 e^-, and (ii) H donates 0.6 of 1.0 e^- to O atom. The work function is calculated to be 4.20 eV. Mg(OH)$_2$ has direct band gap of 3.23 eV, 6.51 within GGA and GGA+GW$_0$, respectively. The wide GW$_0$ band gap is close to the value that was previously obtained [41]. The SO splitting at the Γ is 25 meV, which is slightly larger than that of h-AlN (15 meV). This small difference can be understood from the difference between the atomic radius of N and O atoms.

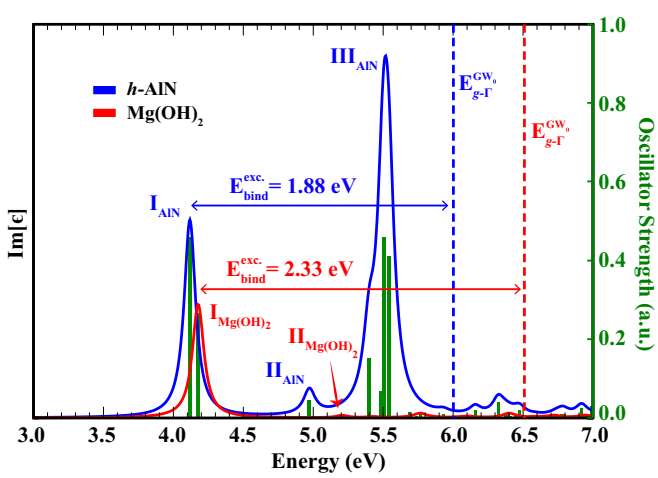

FIG. 2. The imaginary part of the dielectric function of h-AlN (blue curve) and Mg(OH)$_2$ (red curve) with oscillator strength of excitonic states (vertical green lines). The first, second, and third excitons are labeled as I, II, III with the subscript of the corresponding individual layer, respectively. The quasiparticle band gap of h-AlN (blue dashed) and Mg(OH)$_2$ (red dashed) at Γ and exciton binding energies ($E_{bind}^{exc.}$) are given.

In Fig. 2, the energy dependency of the imaginary part of the dielectric function of pristine h-AlN and Mg(OH)$_2$ are shown. We name the peaks as I, II, and III (first, second, and third, respectively) with the subscript that specify the corresponding individual layer. The I_{AlN} appears at 4.12 eV with the exciton binding energy of 1.88 eV. The II_{AlN} and III_{AlN} appear at 4.97 and 5.4 eV, respectively. The III_{AlN} consists of four exciton levels. The $I_{Mg(OH)_2}$ and $II_{Mg(OH)_2}$ appear at 4.18 and 5.20 eV, respectively. The excitonic binding energy of the $I_{Mg(OH)_2}$ is found to be 2.33 eV. The peaks of the h-AlN are larger than those of Mg(OH)$_2$. The reason is that all the peaks shown in Fig. 2 originate from the excitation at the Γ, hence the overlapping of electron and hole states are larger for the h-AlN, which is clearly seen at the charge density of band edges in Fig. 1. In addition, the excitonic binding energies are larger compared to the bulk materials. Such binding energies were previously reported and discussed [53–55].

IV. BILAYER HETEROSTRUCTURE

In this section, we give an analysis of structural, electronic, and optical properties of bilayer heterostructure of vertically stacked monolayer h-AlN and Mg(OH)$_2$.

A. Determination of stacking type

First of all, to determine energetically favorable structure, six different stacking orders are considered. As shown in Fig. 3(a), possible stacking orders are AA (Al on Mg, N on H), AA' (N on Mg, Al on H), AB (Al on H, N at the midpoint of three H), AB' (N on H, Al at the midpoint of three H), AC (Al and N on top of midpoint of H triangles and N on Mg), and AC' (switched of Al and N form of AC). The energy difference between different stackings are given in Table II. In general, the heterobilayer has three types of properties with respect to localization of Al or N on trigonal H surface of Mg(OH)$_2$; when N atom is on top of H atom, which means the AB' and AA stacking types, the heterobilayers possess the lowest energies with highest binding energies. They have also similar band gap of 2.30 and 2.31 eV, respectively. The work functions are found to be 4.31 and 4.32 eV, which are very close to each other. Instead of these energetically favorable forms, the minimum interlayer distances are obtained when the Al and N atoms coincide to the midpoint H triangles (AC' and AC'). The band gap and work function values of the AC' and AC' stacking are found to be similar as well. When Al is on top of H, the structures have the highest interlayer distances highest energy and lowest binding energy. The AA with AB', AA' with AB, and AC with AC' have similar parameters.

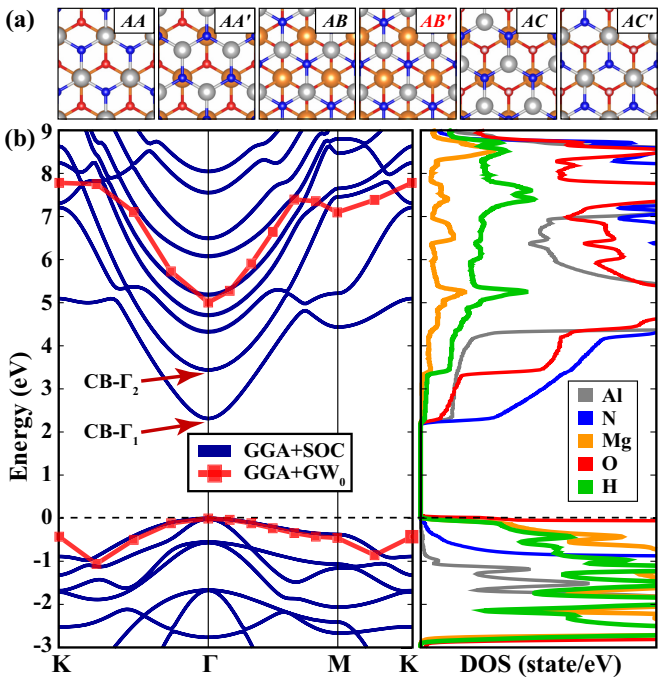

FIG. 3. (a) Top view of six different stacking orders, (b) Electronic band dispersion (left panel) and the partial density of state (right panel) of AB' stacking order which is the most favorable stacking order. The CB-Γ_1 and CB-Γ_2 label the first and second lowest levels of the CB at Γ point, respectively.

The minimum energy of the heterobilayer is obtained when the layers are stacked in the form of AB' stacking, which exhibits the maximum interlayer interaction of 237 meV. Interlayer distance, which is defined as the perpendicular distance from surface H atom to the h-AlN plane, is 2.13 Å. The work function of $Mg(OH)_2$ side is calculated to be 4.31 eV. The VBM and CBM are at Γ as in monolayer $Mg(OH)_2$; however, the band gap values of 2.30 eV within GGA are significantly low compared to that of monolayer of h-AlN and $Mg(OH)_2$. In addition, the AA stacking order is energetically very close to AB'. For both AB' and AA, the layer-layer interaction, interlayer distances, and also band gap values are almost same.

TABLE II. The stacking labels are given in the first column. Calculated parameters for bilayer heterostructure of h-AlN and $Mg(OH)_2$ are the interlayer distance, $d_{L\text{-}L}$; the energy difference between the ground state, Δ_E; the interaction energy between the layers, E_{int}; and the work function Φ. E_g^{GGA} are the energy band gap values within GGA+SOC.

	$d_{L\text{-}L}$ (Å)	Δ_E (meV)	E_{int} (meV)	Φ (eV)	E_g^{GGA} (eV)
AB'	2.13	0	237	4.31	2.30
AA	2.12	6	231	4.32	2.31
AC	2.06	66	171	4.70	2.65
AC'	2.10	76	161	4.69	2.61
AA'	2.75	162	75	4.35	2.14
AB	2.75	164	73	4.29	2.14

In addition, considering vacuum level positions, formation of a staggered gap, with a mismatch of 1.02 eV at the intimate contact point of monolayers is predicted. Moreover, Since the minimum energy difference between the VB and CB is at Γ point [see Fig. 3(b)], the lower energy optical activity takes place at this high symmetry point of Brillouin Zone. Such a contact between two atomically flat surfaces forms an ultraclean Type-II heterojunction.

B. Origin of excitonic states of bilayer heterostructure

In this section, the origin of the prominent excitonic peaks in the AlN/$Mg(OH)_2$ heterobilayer structure, which corresponds to the AB′ stacking, are investigated in detail. There are two effects that determine characteristic properties of exciton in two-dimensional materials: the dielectric screening and the structural confinement. In general, when the crystal structure of a usual semiconductor is reduced from 3D to 2D, the dielectric screening between electron and hole takes place only inside layer. Therefore, as a consequence of the dimensional reduction, the screening effect on electron-hole pair is lower for 2D crystals as compared to the bulk.

In Fig. 4, we show interlayer-spacing-dependent excitonic properties to investigate the origin and evolution of the excitons by tracking their peak positions and corresponding oscillator strengths in the energy spectrum.

As shown in Fig. 4(a), starting from the interlayer spacing of 6.0 Å (equilibrium distance is set to 0 Å), the first peak of the isolated $Mg(OH)_2$ splits into two different peaks due to the broken symmetry of the top and bottom surface charge densities. It is seen that the first peak of the bilayer structure, $\mathbf{I_{bil}}$, appears at the lower energy level than the first peak of both individual h-AlN and $Mg(OH)_2$. As calculated in the previous section, the VBM and CBM electronic states are

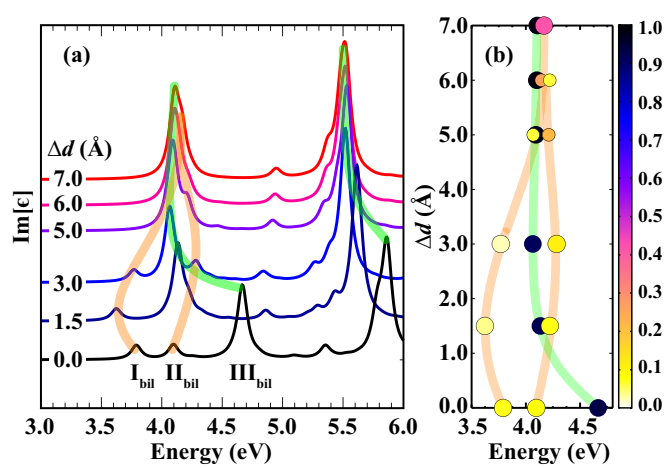

FIG. 4. (a) The imaginary part of the dielectric functions of the AB' stacked heterobilayer are shown for different interlayer distances starting from ground state distance of 2.13 Å. Δd refers to interlayer distance while the ground state distance is set to 0 and labeled as 0.0 Å. The lowest three exciton peaks are labeled as $\mathbf{I_{bil}}$, $\mathbf{II_{bil}}$, and $\mathbf{III_{bil}}$. (b) The distance dependent oscillator strengths of lowest three excitons are shown. Color code is given. The position of the prominent peaks are illustrated by shaded curves. The length of the out-of-plane lattice vector is fixed for different interlayer distance.

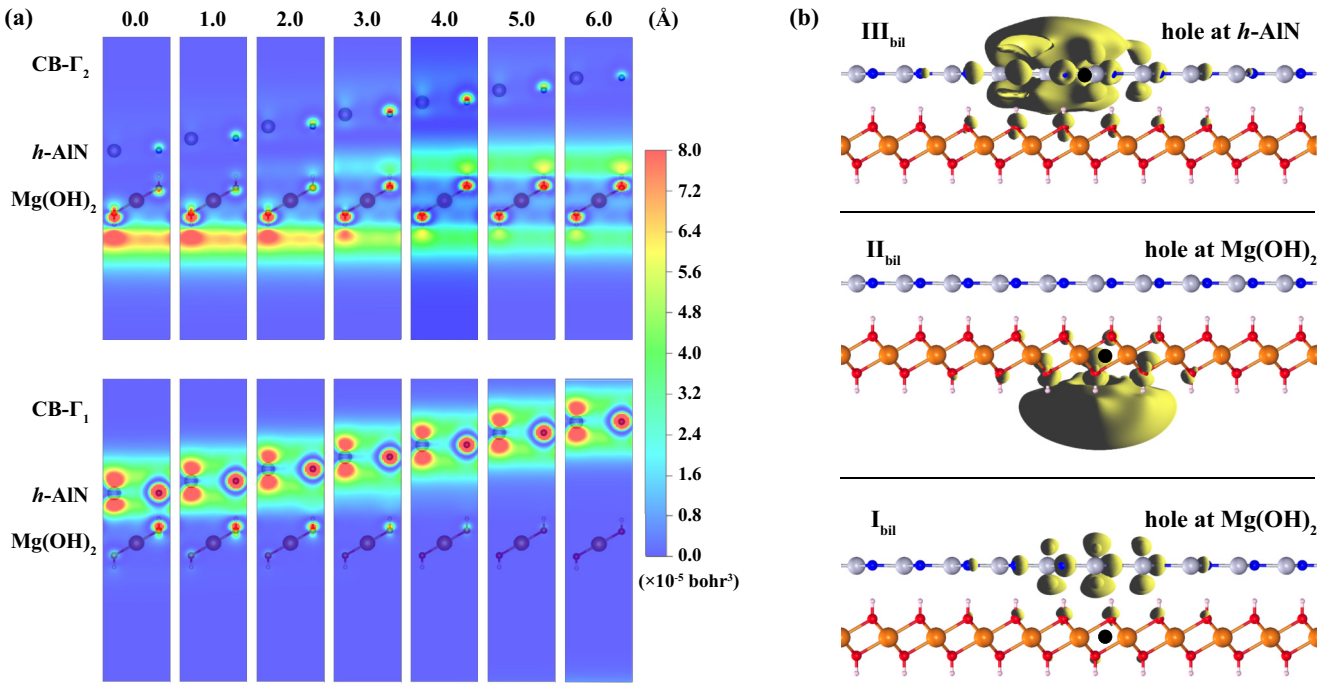

FIG. 5. (a) Layer-layer distance dependent band decomposed charge densities at the Γ point for the lowest two bands (CB-Γ_1 and CB-Γ_2) are presented. The numbers on the upper part of the figure are distances between the layers in the unit of Å. The optimized layer-layer distance is set to 0.0 Å. (b) The wave function of the lowest three excitons, which are labeled as $\mathbf{I_{bil}}$, $\mathbf{II_{bil}}$, and $\mathbf{III_{bil}}$. The yellow regions are the probability of the electron localization when the hole is at a specific point. The position of holes are shown as a black point on the structures for all wave functions. The methodology for the determination of excitonic wave functions is given in Appendix B.

mainly formed by the O and N, respectively. Therefore, the first peak of the bilayer heterostructure, $\mathbf{I_{bil}}$, corresponds to a spatially indirect exciton in which the electron localizes at the N of h-AlN and the hole is at O of Mg(OH)$_2$. As shown in Fig. 4(b), the reduction in the oscillator strength of $\mathbf{I_{bil}}$ (minimum of all) at around 3.0 Å reveals that electronic state of Mg(OH)$_2$ at the intimate contact surface overlaps with h-AlN layer as the distance decreases. However, at the optimum interlayer distance, other Mg(OH)$_2$-originated exciton state evolves into the second peak of the heterostructure labeled as $\mathbf{II_{bil}}$. Apparently, the electronic state of $\mathbf{II_{bil}}$ exciton peak originates from the outer surface state of Mg(OH)$_2$.

On the other hand, the origin and interlayer-spacing-dependence of $\mathbf{III_{bil}}$, differs from those of $\mathbf{I_{bil}}$ and $\mathbf{II_{bil}}$. First, in Fig. 4 it is evident that by decreasing interlayer spacing the first excitonic peak of h-AlN crystal gradually evolves into third state of hetero-bilayer, labeled as $\mathbf{III_{bil}}$. It is seen from Figs. 4(a) and 4(b) that the shape and the oscillator strength of the $\mathbf{III_{bil}}$ do not change significantly. Therefore, one can conclude that the characteristic properties of the $\mathbf{III_{bil}}$ are almost the same as the first excitonic state of h-AlN monolayer crystal. When the distance decrease under 4.0 Å, a significant charge distribution appears on the O atom. It appears that the screening on the h-AlN increases when the Mg(OH)$_2$ layers become closer. Therefore, as a consequence of decrease in exciton binding energy, the corresponding peak shows a significant blue shift.

For a deeper understanding of nature of excitonic states of the vdW Mg(OH)$_2$/h-AlN heterostructure we also investigate the band decomposed charge densities and exctionic wave functions. In Fig. 5(a), the interlayer-spacing-dependent band decomposed charge densities of the lowest and second-lowest levels of the CB at Γ point are shown. The lowest and second-lowest levels are labeled as CB-Γ_1 and CB-Γ_2, respectively. The changes in the charge densities of these two levels contain remarkable information about the evolution of the electrons involved in the states $\mathbf{I_{bil}}$, $\mathbf{II_{bil}}$, and $\mathbf{III_{bil}}$.

First, when the distance is 6.0 Å, the charge density shown in CB-Γ_2 part of the Fig. 5(a) corresponds to the charge density at the CBM of individual Mg(OH)$_2$. It is seen that this density appears mostly on O atoms and also at the surfaces of the Mg(OH)$_2$. As the interlayer distance decreases, the charge density vanishes at the inner surface and increases at the outer surface. On the other hand, the density shown in the CB-Γ_1 for the interlayer distance of 6.0 Å corresponds to the charge density at the CBM of individual h-AlN. As the distance decreases, charge changes negligibly at the vicinity of h-AlN but an additional charge density appears on inner O atom when the distance is less than 4.0 Å. It appears that when the layers approach each other, the inner surface electron of the Mg(OH)$_2$ is transferred to the h-AlN, and the outer surface electron states of the Mg(OH)$_2$ remains at its original position.

Furthermore, we also calculate the real space exciton localizations by using the methodology given in Appendix B. The wave functions of the $\mathbf{I_{bil}}$, $\mathbf{II_{bil}}$, and $\mathbf{III_{bil}}$ are shown in Fig. 5(b) where the yellow regions correspond to electrons and the black points stand for holes. As shown in the lower panel, it is evident that the $\mathbf{I_{bil}}$ is the spatially indirect exciton in which the electron and hole localize on the h-AlN and Mg(OH)$_2$, respectively. The $\mathbf{II_{bil}}$ localizes at the outer side of

the $Mg(OH)_2$ as shown in middle panel of the Fig. 5(b). It seems that the $\mathbf{II_{bil}}$ is not affected by the h-AlN. The $\mathbf{III_{bil}}$ shown in the upper panel of the Fig. 5(b) stays mostly on the h-AlN. A small portion of the $\mathbf{III_{bil}}$ appears on the hydroxide regions of the $Mg(OH)_2$.

V. CONCLUSION

In this study, structural, electronic, and optical properties of the recently synthesized novel 2D materials of h-AlN and $Mg(OH)_2$ and their bilayer heterostructure are investigated by performing DFT calculation. The excitonic states are also calculated by solving BSE over the GW_0 approximation on top of DFT. Our investigation revealed that: (i) the individual monolayer of the h-AlN and $Mg(OH)_2$ can form a vertically stacked heterobilayer; (ii) when the heterobilayer formed, although the interlayer interaction is weak novel exciton states appear; (iii) while h-AlN-states have weak spacing dependence, $Mg(OH)_2$ states are strongly affected by the presence of a neighboring layer; (iv) exponential increase in screening of $Mg(OH)_2$ on h-AlN-states was also predicted; (v) while the first exciton peak is a spatially indirect one, the second and third exciton states are spatially direct states.

Although the constituents have limited optical activity, the heterostructure shows unexpected optical properties. In particular, h-AlN-$Mg(OH)_2$ heterobilayer exhibits spatially indirect excitons, which is important for the optoelectronic application, especially based on photoexcited electron collecting.

ACKNOWLEDGMENTS

The calculations were performed at TUBITAK ULAKBIM, High Performance and Grid Computing Center (TR-Grid e-Infrastructure). C.B. and R.T.S. acknowledge the support from TUBITAK Project No. 114F397. H.S. acknowledges support from Bilim Akademisi—The Science Academy, Turkey, under the BAGEP program. H.S. acknowledges financial support from the Scientific and Technological Research Council of Turkey (TUBITAK) under Project No. 116C073. A.R. and A.D. acknowledge financial support from the European Research Council (Grant No. ERC-2015-AdG-694097), Spanish Grant No. FIS2013-46159-C3-1-P, Grupos Consolidados (Grant No. IT578-13), and AFOSR Grants No. FA2386-15-1-0006 AOARD 144088, No. H2020-NMP-2014, Project MOSTOPHOS (Grant No. 646259), and COST Action Grant No. MP1306 (EUSpec).

APPENDIX A: CONVERGENCE TESTS

Theoretical results on optical properties, especially many-body and excitonic effects, are strongly dependent on computational parameters such as Brillouin zone sampling and the vacuum spacing between the adjacent layers. The calculation with fine parameters, on the other hand, requires large computational resource and time. Therefore, we performed calculations to examine the convergence of the frequency dependent imaginary dielectric function with respect to k-point sampling and the vacuum spacing.

The imaginary part of the dielectric function for the monolayer h-AlN and $Mg(OH)_2$ with respect to k-point sampling are shown in Figs. 6(a) and 6(b), respectively. When the number of k-points increases, the spectrum of both monolayers are blue-shifted and rapidly converges by the $12\times12\times1$ sampling [see Fig. 6(c)]. Therefore, using $12\times12\times1$ for optical properties of monolayer h-AlN and $Mg(OH)_2$ provides reliable results.

As shown in Figs. 7(a) and 7(b), the effect of the vacuum spacing is also evident that the peak positions of both monolayers are red-shifted. For the h-AlN, the curves of

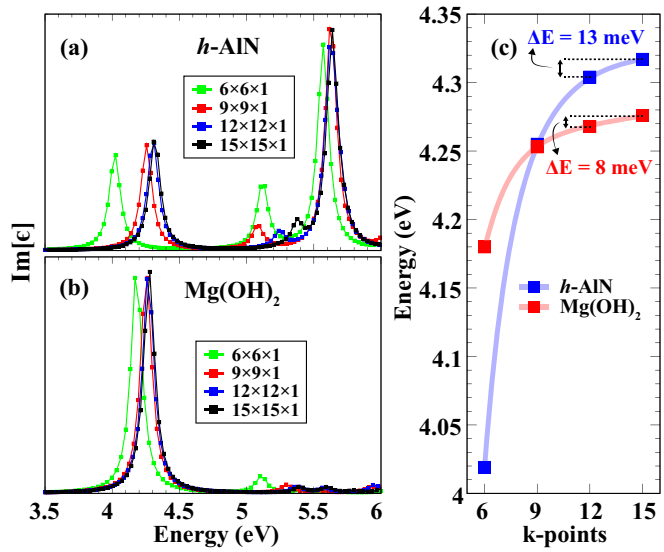

FIG. 6. The results of the k-point sampling tests: (a, b) the imaginary part of the dielectric functions of the monolayer h-AlN and $Mg(OH)_2$ for different k-point samplings, respectively; (c) the first exciton peak positions are shown as the blue and red squares for the monolayer h-AlN and $Mg(OH)_2$, respectively.

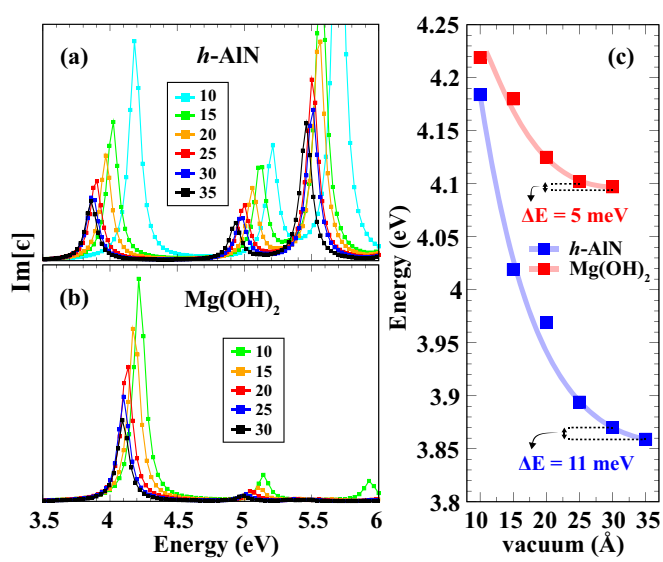

FIG. 7. The results of vacuum spacing tests: (a, b) the imaginary part of the dielectric functions of the monolayer h-AlN and $Mg(OH)_2$ for different vacuum spacing values, respectively; (c) the first exciton peak positions are shown. The blue and red curves correspond to the monolayer h-AlN and $Mg(OH)_2$, respectively.

30 and 35 Å vacuum spacing values are almost the same. For Mg(OH)$_2$, the curve does not change significantly when the vacuum spacing increases from 25 to 30 Å. Moreover, as shown in Fig. 7(c), the difference between the first exciton energies of 30 and 35 Å vacuum spacing values is 11 meV for the monolayer h-AlN. The smaller energy difference of 5 meV is obtained between 25 and 30 Å vacuum spacing values for the monolayer Mg(OH)$_2$. It is clearly seen that the vacuum spacing of 30 and 25 Å are sufficient for the monolayers h-AlN and Mg(OH)$_2$, respectively. Therefore, when we consider the heterobilayer, using the vacuum spacing of ∼28 Å for optical properties provides reliable results. After having convergence tests, the best parameter set of $12\times12\times1$ k-point and 28 vacuum spacings are used in our calculations.

APPENDIX B: METHODOLOGY FOR DETERMINATION OF EXCITONIC WAVE FUNCTIONS

For a deeper understanding of the origin of excitonic states and determination of their wave functions of the vdW heterobilayer, three lowest exciton wave functions were calculated by using BERKELEYGW package [56] on top of QUANTUMESPRESSO code [57]. The eigenvalues and the eigenfunctions in the independent particle picture were obtained by using PBE form of GGA for exchange and correlation. The quasiparticle energies were calculated within the GW approximation. We employed an energy cutoff of 160 Ry for the PBE calculations. For the computation of the dielectric matrix, we used 1987 conduction bands and G-vectors with energy up to 17 Ry, whereas the self-energy operator was computed using 1987 conduction bands and a G-vector cutoff of 17 and 160 Ry for the screened and bare Coulomb matrices, respectively. To sample the BZ we employed a $6\times6\times1$ k-point grid for the PBE and GW calculations, whereas for the solution of the BSE, we used a $18\times18\times3$ k-point grid with linearly interpolated GW quasiparticles energies. The eight lowest conduction bands and eight topmost valence bands were included to solve the BSE. After obtaining the excitonic states, the probability of localization of the electron is calculated for each excitonic level when the hole is fixed to a specific point. The result are given in Fig. 5(b).

[1] K. S. Novoselov, A. K. Geim, S. V. Morozov, D. Jiang, Y. Zhang, S. V. Dubonos, I. V. Grigorieva, and A. A. Firsov, Science **306**, 666 (2004).

[2] K. S. Novoselov, D. Jiang, F. Schedin, T. J. Booth, V. V. Khotkevich, S. V. Morozov, and A. K. Geim, Proc. Natl. Acad. Sci. USA **102**, 10451 (2005).

[3] S. Z. Butler, S. M. Hollen, L. Cao, Y. Cui, J. A. Gupta, H. R. Gutiérrez, T. F. Heinz, S. S. Hong, J. Huang, A. F. Ismach, E. Johnston-Halperin, M. Kuno, V. V. Plashnitsa, R. D. Robinson, R. S. Ruoff, S. Salahuddin, J. Shan, L. Shi, M. G. Spencer, M. Terrones, W. Windl, and J. E. Goldberger, ACS Nano **7**, 2898 (2013).

[4] M. Chhowalla, H. S. Shin, G. Eda, L.-J. Li, K. P. Loh, and H. Zhang, Nat. Chem. **5**, 263 (2013).

[5] S. Cahangirov, M. Topsakal, E. Akturk, H. Sahin, and S. Ciraci, Phys. Rev. Lett. **102**, 236804 (2009).

[6] A. Kara, H. Enriquez, A. P. Seitsonen, L. C. L. Y. Voon, S. Vizzini, B. Aufray, and Hamid Oughaddou, Surf. Sci. Rep. **67**, 1 (2012).

[7] G. G. Guzman-Verri and L. C. Lew Yan Voon, Phys. Rev. B **76**, 075131 (2007).

[8] F. Bechstedt, L. Matthes, P. Gori, and O. Pulci, Appl. Phys. Lett. **100**, 261906 (2012).

[9] R. A. Gordon, D. Yang, E. D. Crozier, D. T. Jiang, and R. F. Frindt, Phys. Rev. B **65**, 125407 (2002).

[10] J. N. Coleman, M. Lotya, A. O'Neill, S. D. Bergin, P. J. King, U. Khan, K. Young, A. Gaucher, S. De, R. J. Smith, I. V. Shvets, S. K. Arora, J. J. Boland, J. J. Wang, J. F. Donegan, J. C. Grunlan, G. Moriarty, A. Shmeliov, R. J. Nicholls, J. M. Perkins, E. M. Grieveson, K. Theuwissen, D. W. McComb, P. D. Nellist, and V. Nicolosi, Science **331**, 568 (2011).

[11] Q. H. Wang, K. Kalantar-Zadeh, A. Kis, J. N. Coleman, and M. S. Strano, Nat. Nanotechnol. **7**, 699 (2012).

[12] J. S. Ross, P. Klement, A. M. Jones, N. J. Ghimire, J. Yan, D. G. Mandrus, T. Taniguchi, K. Watanabe, K. Kitamura, W. Yao, D. H. Cobden, and X. Xu, Nat. Nanotechnol. **9**, 268 (2014).

[13] H. Sahin, S. Tongay, S. Horzum, W. Fan, J. Zhou, J. Li, J. Wu, and F. M. Peeters, Phys. Rev. B **87**, 165409 (2013).

[14] S. Tongay, H. Sahin, C. Ko, A. Luce, W. Fan, K. Liu, J. Zhou, Y.-S. Huang, C.-H. Ho, J. Yan, D. F. Ogletree, S. Aloni, J. Ji, S. Li, J. Li, F. M. Peeters, and J. Wu, Nat. Commun. **5**, 3252 (2014).

[15] S. Horzum, D. Cakir, J. Suh, S. Tongay, Y.-S. Huang, C.-H. Ho, J. Wu, H. Sahin, and F. M. Peeters, Phys. Rev. B **89**, 155433 (2014).

[16] B. Chen, H. Sahin, A. Suslu, L. Ding, M. I. Bertoni, F. M. Peeters, and S. Tongay, ACS Nano **9**, 5326 (2015).

[17] H. Sahin, S. Cahangirov, M. Topsakal, E. Bekaroglu, E. Akturk, R. T. Senger, and S. Ciraci, Phys. Rev. B **80**, 155453 (2009).

[18] Q. Wang, Q. Sun, P. Jena, and Y. Kawazoe, ACS Nano **3**, 621 (2009).

[19] K. K. Kim, A. Hsu, X. Jia, S. M. Kim, Y. Shi, M. Hofmann, D. Nezich, J. F. Rodriguez-Nieva, M. Dresselhaus, T. Palacios, and J. Kong, Nano Lett. **12**, 161 (2012).

[20] P. Tsipas, S. Kassavetis, D. Tsoutsou, E. Xenogiannopoulou, E. Golias, S. A. Giamini, C. Grazianetti, D. Chiappe, A. Molle, M. Fanciulli, and A. Dimoulas, Appl. Phys. Lett. **103**, 251605 (2013).

[21] C. Bacaksiz, H. Sahin, H. D. Ozaydin, S. Horzum, R. T. Senger, and F. M. Peeters, Phys. Rev. B **91**, 085430 (2015).

[22] A. Geim and I. Grigorieva, Nature (London) **499**, 419 (2013).

[23] L. Britnell, R. Gorbachev, R. Jalil, B. Belle, F. Schedin, A. Mishchenko, T. Georgiou, M. Katsnelson, L. Eaves, and S. Morozov, Science **335**, 947 (2012).

[24] H. Fang, C. Battaglia, C. Carraro, S. Nemsak, B. Ozdol, J. S. Kang, H. A. Bechtel, S. B. Desai, F. Kronast, and A. A. Unal, Proc. Natl. Acad. Sci. USA **111**, 6198 (2014).

[25] C.-H. Lee, G.-H. Lee, A. M. van der Zande, W. Chen, Y. Li, M. Han, X. Cui, G. Arefe, C. Nuckolls, and T. F. Heinz, Nat. Nanotechnol. **9**, 676 (2014).

[26] B. Hunt, J. Sanchez-Yamagishi, A. Young, M. Yankowitz, B. J. LeRoy, K. Watanabe, T. Taniguchi, P. Moon, M. Koshino, and P. Jarillo-Herrero, Science **340**, 1427 (2013).
[27] X. Hong, J. Kim, S.-F. Shi, Y. Zhang, C. Jin, Y. Sun, S. Tongay, J. Wu, Y. Zhang, and F. Wang, Nat. Nanotechnol. **9**, 682 (2014).
[28] A. C. Ferrari *et al.*, Nanoscale **7**, 4598 (2015).
[29] C. L. Tan and H. Zhang, Chem. Soc. Rev. **44**, 2713 (2015).
[30] E. F. de Almeida Junior, F. de Brito Mota, C. M. C. de Castilho, A. Kakanakova-Georgieva, and G. K. Gueorguiev, Eur. Phys. J. B. **85**, 48 (2012).
[31] C. Shi, H. Qin, Y. Zhang, J. Hu, and L. Ju, J. Appl. Phys. **115**, 053907 (2014).
[32] F. L. Zheng, J. M. Zhang, Y. Zhang, and V. Ji, Physica B **405**, 3775 (2010).
[33] D. Kecik, C. Bacaksiz, R. T. Senger, and E. Durgun, Phys. Rev. B **92**, 165408 (2015).
[34] S. Utamapanya, K. J. Klabunde, and J. R. Schlup, Chem. Mater. **3**, 175 (1991).
[35] Y. Ding, G. Zhang, H. Wu, B. Hai, L. Wang, and Y. Qian, Chem. Mater. **13**, 435 (2001).
[36] P. J. Sideris, U. G. Nielsen, Z. Gan, and C. P. Grey, Science **321**, 113 (2008).
[37] T. Murakami, T. Honjo, and T. Kuji, Mater. Trans. **52**, 1689 (2011).
[38] Y. Aierken, H. Sahin, F. Iyikanat, S. Horzum, A. Suslu, B. Chen, R. T. Senger, S. Tongay, and F. M. Peeters, Phys. Rev. B **91**, 245413 (2015).
[39] E. Torun, H. Sahin, and F. M. Peeters, Phys. Rev. B **93**, 075111 (2016).
[40] A. A. Tsukanov and S. G. Psakhie, Sci. Rep. **6**, 19986 (2016).
[41] A. Suslu, K. Wu, H. Sahin, B. Chen, S. Yang, H. Cai, T. Aoki, S. Horzum, J. Kang, F. M. Peeters, and S. Tongay, Sci. Rep. **6**, 20525 (2016).
[42] M. Yagmurcukardes, E. Torun, R. T. Senger, F. M. Peeters, and H. Sahin, Phys. Rev. B **94**, 195403 (2016).
[43] G. Kresse and J. Hafner, Phys. Rev. B **47**, 558 (1993).
[44] G. Kresse and J. Furthmuller, Phys. Rev. B **54**, 11169 (1996).
[45] G. Kresse and D. Joubert, Phys. Rev. B **59**, 1758 (1999).
[46] J. P. Perdew, K. Burke, and M. Ernzerhof, Phys. Rev. Lett. **77**, 3865 (1996).
[47] S. J. Grimme, Comput. Chem. **27**, 1787 (2006).
[48] T. Bucko, J. Hafner, S. Lebegue, and J. G. Angyan, J. Phys. Chem. A **114**, 11814 (2010).
[49] R. F. W. Bader, *Atoms in Molecules: A Quantum Theory* (Oxford University Press, Oxford, UK, 1990).
[50] H. Bethe and E. Salpeter, Phys. Rev. **84**, 1232 (1951).
[51] W. Hanke and L. J. Sham, Phys. Rev. B **21**, 4656 (1980).
[52] K. F. Mak, C. Lee, J. Hone, J. Shan, and T. F. Heinz, Phys. Rev. Lett. **105**, 136805 (2010).
[53] L. Wirtz, A. Marini, and A. Rubio, Phys. Rev. Lett. **96**, 126104 (2006).
[54] A. Pishtshev, S. Zh. Karazhanov, and M. Klopov, Solid State Commun. **193**, 11 (2014).
[55] P. Cudazzo, L. Sponza, C. Giorgetti, L. Reining, F. Sottile, and M. Gatti, Phys. Rev. Lett. **116**, 066803 (2016).
[56] J. Deslippe, G. Samsonidzea, D. A. Strubbea, M. Jaina, and M. L. Cohen, Comput. Phys. Commun. **183**, 1269 (2012).
[57] P. Giannozzi, S. Baroni, N. Bonini, M. Calandra, R. Car, C. Cavazzoni, D. Ceresoli, G. L. Chiarotti, M. Cococcioni, I. Dabo, A. D. Corso, S. de Gironcoli, S. Fabris, G. Fratesi, R. Gebauer, U. Gerstmann, C. Gougoussis, A. Kokalj, M. Lazzeri, L. Martin-Samos, N. Marzari, F. Mauri, R. Mazzarello, S. Paolini, A. Pasquarello, L. Paulatto, C. Sbraccia, S. Scandolo, G. Sclauzero, A. P. Seitsonen, A. Smogunov, P. Umari, and R. M. Wentzcovitch, J. Phys.: Condens. Matter **21**, 395502 (2009).